Bioconjugate Chemistry

Article

Synthesis and Evaluation of Manganese (II)-based Ethylenediaminetetraacetic Acid-Ethoxybenzyl Conjugate as a Highly Stable Hepatobiliary Magnetic Resonance Imaging Contrast Agent

Md. Kamrul Islam, Soyeon Kim, Hee-Kyung Kim, Yeoun-Hee Kim, Young-Mi Lee, Garam Choi, Ah Rum Baek, Bo Kyung Sung, Minsup Kim, Art E. Cho, Hyo Jeung Kang, Gang-Ho Lee, Seon Hee Choi, Taekwan Lee, Ji Ae Park, and Yongmin Chang

Bioconjugate Chem., **Just Accepted Manuscript** • DOI: 10.1021/acs.bioconjchem.8b00560 • Publication Date (Web): 01 Nov 2018

ACS Publications

is published by the American Chemical Society. 1155 Sixteenth Street N.W., Washington, DC 20036

Synthesis and Evaluation of Manganese (II)-based Ethylenediaminetetraacetic Acid-Ethoxybenzyl Conjugate as a Highly Stable Hepatobiliary Magnetic Resonance Imaging Contrast Agent

Md. Kamrul Islam,[a,†] Soyeon Kim,[a,†] Hee-Kyung Kim,[b,c] Yeoun-Hee Kim,[d] Young-Mi Lee,[c] Garam Choi,[a] Ah Rum Baek,[a] Bo Kyung Sung,[a] Minsup Kim,[e] Art E. Cho,[e] Hyojeung Kang,[f] Gang-Ho Lee,[g] Seon Hee Choi,[h] Taekwan Lee,[h] Ji-Ae Park,[i] and Yongmin Chang[j,k,*]

[a]Department of Medical & Biological Engineering, [f]Department of Pharmacy, [g]Department of Chemistry, Kyungpook National University, 80, Daehak-ro, Buk-gu, Daegu 41566, Korea

[b]BK21 Plus KNU Biomedical Convergence Program, School of Medicine, [c]Institute of Biomedical Engineering Research, [j]Department of Molecular Medicine, School of Medicine, Kyungpook National University, 680, Gukchaebosang-ro, Jung-gu, Daegu 41944, Korea

[d]Institute of New Drug Research, Myungmoon Bio, 180, Yuram-ro, Dong-gu, Daegu, 41059, Korea.

[e]Department of Bioinformatics, Korea University Sejong Campus, 2511, Sejong-ro, Sejong city, 30019, Korea.

[h]Laboratory Animal Center, Daegu-Gyeongbuk Medical Innovation Foundation, 80, Chumbok-ro, Dong-gu, Daegu 41061, Korea

[i]Molecular Imaging Research Center, Korea Institute of Radiological and Medical Sciences, Seoul 139-706, Korea

[k]Department of Radiology, Kyungpook National University Hospital, 130 Dongdeok-ro, Jung-gu, Daegu 41944, Korea

† These authors contributed equally to this article.

* Corresponding author: E-mail: ychang@knu.ac.kr

ABSTRACT

In this study, we designed and synthesized a highly stable manganese (Mn^{2+})-based hepatobiliary complex by tethering an ethoxybenzyl (EOB) moiety with an ethylenediaminetetraacetic acid (EDTA) coordination cage as an alternative to the well-established hepatobiliary gadolinium (Gd^{3+}) chelates and evaluated its usage as a T_1 hepatobiliary magnetic resonance imaging (MRI) contrast agent (CA). This new complex exhibits higher r_1 relaxivity (2.3 mM^{-1} s^{-1}) than clinically approved Mn^{2+}-based hepatobiliary complex Mn-DPDP (1.6 mM^{-1} s^{-1}) at 1.5 T. Mn-EDTA-EOB shows much higher kinetic inertness than that of clinically approved Gd^{3+}-based hepatobiliary MRI CAs, such as Gd-DTPA-EOB and Gd-BOPTA. In addition, *in vivo* biodistribution and MRI enhancement patterns of this new Mn^{2+} chelate are comparable to those of Gd^{3+}-based hepatobiliary MRI CAs. The diagnostic efficacy of the new complex was demonstrated by its enhanced tumor detection sensitivity in a liver cancer model using *in vivo* MRI.

INTRODUCTION

Hepatocellular carcinoma (HCC) is currently one of the leading causes of cancer related death, which represents over 90% of all primary liver cancers.[1] If diagnosis of the HCC is late, malignancy has an unfavorable prognosis. This year, it is estimated that 30,200 deaths (20,540 men and 9,660 women) will occur in the United States by this disease.[2] Early diagnosis and effective treatment can increase the long-term survival rate up to 50%–70% (5-year survival).[3] Thus, liver-specific CAs are important for early diagnosis of the HCC.

Gadolinium (Gd^{3+}) is a popular choice amongst paramagnetic metals used as contrast agents (CAs) for magnetic resonance imaging (MRI) owing to its suitable magnetic properties.[4-6] However, some Gd^{3+}-based imaging probes are associated with the initiation of nephrogenic systemic fibrosis (NSF), a rare but fatal fibrosis of the organs that can arise in patients with compromised renal function.[7,8] Furthermore, a number of reports demonstrated that intravenously administered Gd^{3+}-based imaging agents accumulate in the brains of patients with normal renal function, further questioning the use of certain marketed Gd^{3+}-based CAs.[9-11] Therefore, non-lanthanide metals, particularly less toxic and more biofriendly Mn^{2+}-based complexes, are receiving special attention for the development of next-generation potent MRI-CAs.[12-17]

Mn^{2+} ions with spin number (S = 5/2) possess fast water exchange kinetics and slow longitudinal electronic relaxation, which are necessary physical properties for MR CAs.[18-21] However, Mn^{2+} ions are not free from *in vivo* toxicity. The use of Mn^{2+} ions poses toxicological

concerns because overexposure to this metal ion can lead to progressive and permanent damage to the brain.[22] Although small amounts of Mn^{2+} are required by the human body, overexposure to free Mn^{2+} ions may cause neurotoxicity that can develop into a Parkinson-like disease called manganism.[23] In addition, cardiovascular, liver, as well as reproductive and developmental toxicities have been reported. The typical symptoms of manganism often correlate with the degree of Mn^{2+} ion accumulation in the globus pallidus, which is seen as hyper intensity on a T_1 MRI.[24] Mn-DPDP (mangafodipir trisodium; Chart 1), approved by the food and drug administration **(**FDA) for use as a liver imaging agent, releases free Mn^{2+} ions in the blood vessel after intravenous (IV) administration, which are responsible for T_1 contrast enhancement.[25] Mn-DPDP showed relatively low relaxivity; thus, an increased dose is required to generate sufficient contrast enhancement, and it may lead to unexpected toxic side effects. Although Mn-DPDP is the first liver-specific hepatobiliary MR CA, it is no longer available for clinical use because of low relaxivity and potential safety issues.[26] Therefore, even for Mn^{2+}-based MRI-CAs, the *in vivo* stability of the complex is very important to minimize potential toxicity. Because Mn^{2+} is essential for mitochondrial function and hepatocytes are mitochondria-rich liver cells, Mn^{2+} homeostasis in the liver is very important and all Mn^{2+}-based liver-specific hepatobiliary MRI-CAs require high *in vivo* stability so as to not release free Mn^{2+}.

Numerous efforts have been made to design stable Mn^{2+}-based complexes with reduced toxicity for *in vivo* MRI applications. Zheng et al synthesized three nanoglobular macrocyclic Mn(II) chelate conjugates for use as promising non-Gd MRI CAs.[27] Recently, a fibrin-targeted $[Mn(PyC_3A)(H_2O)]^-$ complex was synthesized by Caravan et al. as a molecular agent for vascular imaging, and it showed high stability at pH 7.4 (log K_{ML} = 11.40).[28] More recently, we

reported a novel Mn(II) chelate of ethylenediaminetetraacetic acid-benzothiazole aniline (EDTA-BTA) conjugate (Chart 1) as a liver-specific agent based on the lipophilic character of BTA moiety, and it showed comparable kinetic inertness to Gd^{3+}-based agents.[29] Compared to Mn-EDTA-BTA, Mn-EDTA-EOB showed high kinetic stability and this high stability will reduce brain accumulation of free manganese ion and thus will reduce possible neurotoxicity such as manganism. Therefore, the design of highly stable hepatobiliary Mn^{2+} complexes still remains a challenge.

In the current study, we introduce a new chelator EDTA-ethoxybenzyl (EOB) (L) that forms a highly inert complex with Mn^{2+}. We designed the highly stable Mn^{2+} chelate based on an EDTA coordination cage bearing an EOB moiety for use as a hepatobiliary agent. EOB is a lipophilic moiety, which was used in the clinically approved Gd-based hepatobiliary agent, Gd-DTPA-EOB (gadolinium ethoxybenzyl diethylenetriamine pentaacetic acid; Chart 1) chelate.[30] Gd-DTPA-EOB showed 50% accumulation in functioning hepatocytes via excretion into the biliary tract and 50% through the kidneys.[26] In the present study, we aimed to design a complex with Mn^{2+} ions, which has higher chelation stability than Gd^{3+}-based liver-specific MRI CAs, such as Gd-DTPA-EOB and Gd-BOPTA. In addition, we expected that the newly synthesized small Mn^{2+} chelate-based hepatobiliary agent showed much higher *in vivo* stability than the recent Mn (II) chelate of EDTA-BTA conjugate. Moreover, computational modeling studies were performed to predict the possible molecular mechanism of hepatocyte uptake of newly synthesized Mn-EDTA-EOB. We demonstrated that this new hepatobiliary Mn chelate is rapidly taken up by liver hepatocytes and excreted through biliary and renal pathways, and is highly promising for clinical liver imaging applications such as liver cancer imaging.

Chart 1. Structure of the compounds discussed in this study.

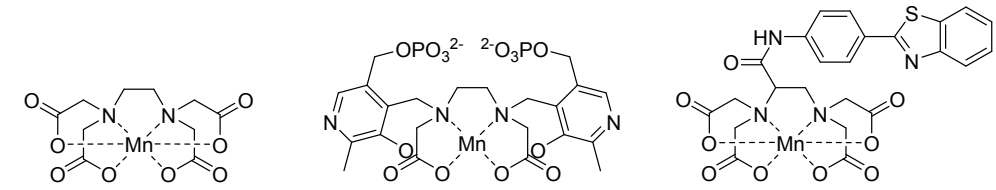

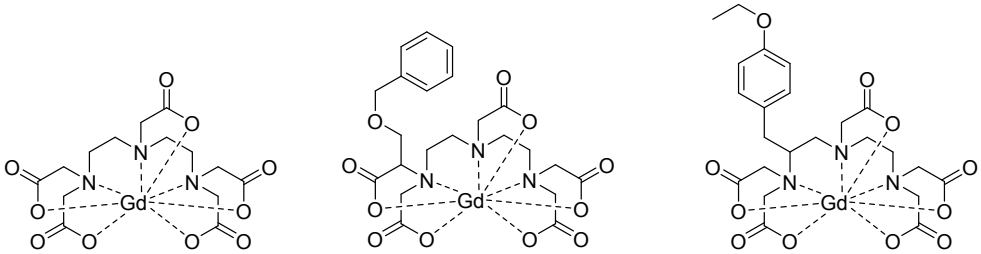

RESULTS AND DISCUSSION

Synthesis and characterization. Scheme 1 shows the procedure for the synthesis of the chelate conjugate and its Mn^{2+} complex (abbreviated as L and Mn-EDTA-EOB, correspondingly). The synthesis of Mn-EDTA-EOB was started from D,L-2,3-diaminopropionic acid monohydrobromide. Compound **1** was synthesized according to a previously published study,[29] and then conjugated with 4-ethoxyaniline in the presence of O-(benzotriazol-1-yl)-N, N, N′, N′-tetramethyluronium hexafluorophosphate (HBTU) to form compound **2** as a white solid. A mixture of trifluoroacetic acid (TFA) and dichloromethane (CH_2Cl_2) was used to cleave *tert*-butyl ester and a pale-yellow product **3** was obtained after precipitation. Alkylation with *tert*-butyl bromoacetate under previously reported conditions resulted in a high yield of the protected EDTA-EOB ligand **4**.[31] Deprotection of the *tert*-butyl group was accomplished using TFA, and the pure ligand L was collected from the reaction mixture as an off-white solid with 53% overall

yield. The Mn^{2+} complex was synthesized by reaction of ligand L with $MnCl_2 \cdot 4H_2O$ (1 equal) at pH 6.5, and the inorganic impurities were removed by using reverse-phase column chromatography. Lyophilization was used to isolate the pure chelate as a sodium salt with 31% overall yield. The ligand formation and its Mn^{2+} complex was evaluated by microanalysis and spectroscopic methods, such as ^1H NMR, HR-FAB-MS, ESI-MS, and elemental analysis (see Supporting Information).

Scheme 1. Synthesis of Mn-EDTA-EOB complex. [a]

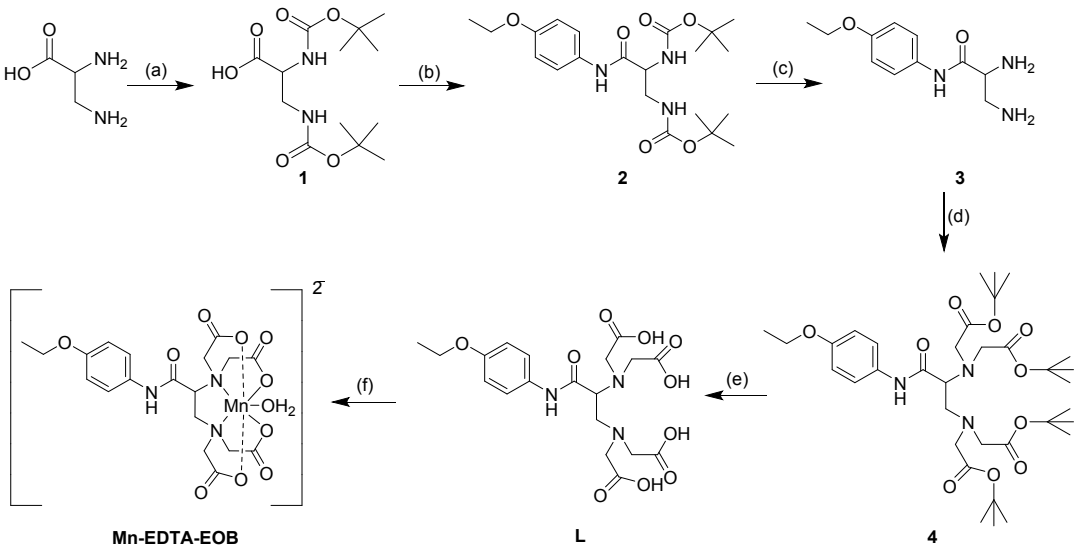

[a] **Reagents and conditions:** (a) $(Boc)_2O$, $NaHCO_3$, 1,4-Dioxane, rt; (b) 4-Ethoxyaniline, DIPEA, HBTU, DMF, rt; (c) TFA, CH_2Cl_2, 0 °C, 18 h; (d) *tert*-Butyl bromoacetate, DIPEA, KI, DMF, 110 °C, 4 h; (e) TFA, CH_2Cl_2, 0 °C, 22 h; (f) $MnCl_2 \cdot 4H_2O$, 1M NaOH, pH 6.5.

Relaxivity and lipophilicity. To understand how the Mn-EDTA-EOB complex acts as a CA for MRI, we compared the relaxivity of Mn-EDTA-EOB with that of Mn-EDTA, Mn-EDTA-BTA, Mn-DPDP, Gd-DTPA, Gd-DTPA-EOB and Gd-BOPTA using a 1.5 T clinical MRI scanner (Table 1). After conjugation with the EOB moiety, r_1 relaxivity of Mn-EDTA-EOB increased approximately 20% compared with that of the parent Mn-EDTA. The lipophilic moiety EOB

might play an important role by slowing down the tumbling rate of Mn-EDTA-EOB and contributing to the high relaxivity.[30,32] In addition, Mn-EDTA-EOB displayed much higher longitudinal relaxivity (r_1) than the clinically approved Mn-DPDP; coordinated inner sphere water might be responsible for this high relaxivity. Subsequently, we also measured relaxivity in an aqueous solution of human serum albumin (HSA) because of the presence of the lipophilic group in the structure of Mn-EDTA-EOB complex. Under this condition, the Mn-EDTA-EOB complex exhibited higher r_1 relaxivity value than Mn-DPDP, demonstrating an interaction between HSA and Mn-EDTA-EOB chelate. When compared with Mn-EDTA-BTA, Mn-EDTA-EOB did not show high r_1 relaxivity as good as Mn-EDTA-BTA. Therefore, Mn-EDTA-EOB is expected to show less contrast enhancement compared to Mn-EDTA-BTA. However, it is also worth to note that overall contrast enhancement is dependent not on r_1 relaxivity but on r_1 /r_2 ratio because r_1 and r_2 enhancements are competitive each other. To estimate the lipophilicity of our synthesized complex, we also determined the octanol-water partitioning coefficient (log P). The log P values are Mn-EDTA-EOB (-2.33), Mn-EDTA (-2.72), Mn-EDTA-BTA (-1.84), and Mn-DPDP (-3.07) (Table 1). The log P value of Mn-EDTA-EOB is 3-fold lower than that of Mn-EDTA-BTA but Mn-EDTA-EOB shows 2.45 and 5.5-fold higher lipophilicity than Mn-EDTA and Mn-DPDP respectively.

Table 1. Relaxivities and octanol-water partition coefficients data of Mn-EDTA-EOB, Mn-EDTA, Mn-EDTA-BTA, Mn-DPDP, Gd-DTPA, Gd-BOPTA and Gd-DTPA-EOB in water, PBS and HSA (64 MHz, 297 K).

Compound	r_1 ($mM^{-1} s^{-1}$)			r_2 ($mM^{-1} s^{-1}$)			r_1/r_2 ratio[g]	$logP_{oct/wat}$
	Water	PBS	HSA[f]	Water	PBS	HSA[f]		
Mn-EDTA-EOB	2.3 ± 0.10	2.4 ±0.11	6.3±0.29	4.3 ± 0.05	4.3 ± 0.04	16.9±0.71	0.53(W) 0.37(H)	−2.33
Mn-EDTA[b]	1.9 ± 0.10	-	-	3.7 ± 0.10	-	-	0.51(W)	−2.72

Mn-EDTA-BTA[b]	3.5 ± 0.10	-	15.1±1.90	4.9 ± 0.10	-	34.5 ± 3.90	0.71(W) 0.43(H)	−1.84
Mn-DPDP[c,d]	1.6± 0.03	2.1± 0.1	5.2± 0.1	2.1± 0.1	2.5± 0.2	8.9± 0.2	0.76(W) 0.58(H)	−3.07
Gd-DTPA[b]	3.3	-	4.3	3.9	-	4.4	0.84(W) 0.97(H)	-3.16
Gd-BOPTA[e]	4.0 ± 0.40	-	-	4.3 ± 1.0	-	-	0.93(W)	-2.23
Gd-DTPA-EOB[e]	4.7 ± 0.40	-	-	5.1 ± 1.2	-	-	0.92(W)	-2.11

[b] Data obtained from ref 29. [c, d] Data obtained from refs 53 and 54. [e]Data obtained from ref 32. [f][HSA] = 0.67 mM in water. [g](W) for r_1/r_2 ratio in water, (H) for r_1/r_2 ratio in HSA solution.

Interaction of Mn-EDTA-EOB complex with HSA. The R_1^{obs} values of a diluted solution of Mn-EDTA-EOB complex were measured to investigate the interaction of the lipophilic Mn-EDTA-EOB complex with HSA. The measurements were performed as a function of protein concentration at the fixed frequency and temperature. R_1^{obs} increases with increasing protein concentrations because the fraction of bound complex, which is characterized by a slower representational motion, increases. The binding constant (K_a) was determined according to a previously published method.[33] Figure 1 shows the results from proton T_1 relaxation rate as a function of Mn-EDTA-EOB concentration at a fixed HSA concentration. The data obtained for Mn-EDTA-EOB offer a relatively sharp inflection point, which is an indication of high stability constant. The binding constant (K_a) of Mn-EDTA-EOB (655 M^{-1}) was much lower than that of the protein binding agent MS-325 (6100 M^{-1}), and there was no obvious brightness observed in blood vessels after injection of Mn-EDTA-EOB to mice (data not shown).[33] Weak protein binding results in increased relaxivity, but does not appear to impact on blood pool contrast.

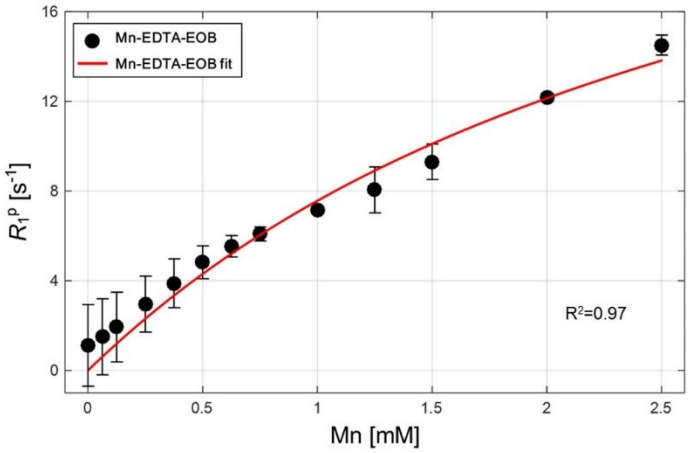

Figure 1. Proton longitudinal paramagnetic relaxation rates of Mn-EDTA-EOB as a function of Mn concentration in aqueous solution of HSA (0.67mM) at 64 MHz and 293 K, fitted using eq 1.

Transmetallation kinetics and pH stability. For safe *in vivo* application, the kinetic stability of CAs is crucial. As the second most abundant transition metal in the human body, divalent zinc (Zn^{2+}) plays a critical role in many cellular processes and can displace more Mn^{2+} than other endogenous metal ions such as Cu^{2+} and Ca^{2+}. Thus, in this study, the stability of the Mn^{2+} complex was measured by determining the transmetallation kinetics of Zn^{2+} ions. Transmetallation rates are frequently characterized by measuring the progress of normalized r_1 or r_2 relaxivities as a function of time.[28,29] The kinetic stability of Mn-EDTA-EOB was characterized by a change in transverse relaxation rate, $\{\Delta R_2(t) = R_2(t) - R_2(0)\}$ of complex incubated with Zn^{2+} (10 equiv.) as a function of time. The kinetic stability of Mn-EDTA, Mn-DPDP, Mn-EDTA-BTA, Gd-DTPA-EOB, and Gd-BOPTA was also tested for comparison (Figure 2). As shown in Figure 2, Mn-EDTA-EOB shows much higher kinetic stability than others for the 72-h experimental period. Although the manganese coordination with EDTA and EDTA-EOB is similar, Mn-EDTA-EOB shows higher transmetallic stability than Mn-EDTA. One possible explanation is that the steric hindrance induced by the EOB group located on the

ethylene bridge might to have a favorable effect by reducing the accessibility of Zn^{2+} and/or by rigidifying the structure of Mn-EDTA-EOB complex.[34] Mn-EDTA-EOB shows higher kinetic inertness [lower $\Delta R_2(t)$ value] than the previously studied Mn^{2+}-based liver-specific agent Mn-EDTA-BTA, demonstrating that EOB has better rigidifying effect than BTA in terms of transmetalation. Furthermore, the kinetic stability of Mn-EDTA-EOB was much higher than that of clinically used Gd-based MRI CAs, such as Gd-DTPA-EOB and Gd-BOPTA. These results indicate that Mn-EDTA-EOB has much higher kinetic inertness toward transmetallation by Zn^{2+}. In addition, stability of the Mn-EDTA-EOB was also measured at various pH range as a function of the time. Little change in relaxivity was observed upon going from basic to acidic pH, suggesting that Mn-EDTA-EOB is stable enough throughout a wide range of pH from 3 to 11 (see Figure S12). Thus, we expect that Mn-EDTA-EOB can be a good alternative to Gd-based CAs, particularly for renally impaired populations where Gd usage carries additional risk. In patients with low glomerular filtration rate (GFR), the Mn-chelate may circulate for extended periods, and we assume that any slowly released Mn^{2+} may be excreted by the liver.

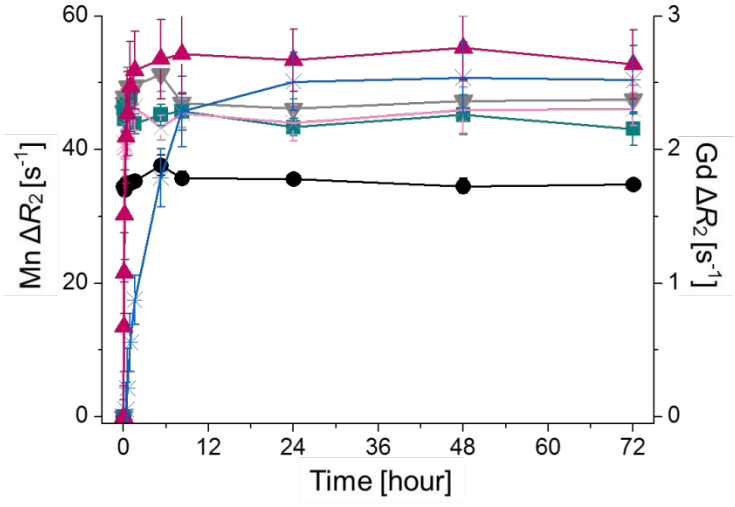

Figure 2. Transmetallation of 1mM Mn-EDTA (▼), Mn-DPDP (X) Mn-EDTA-BTA (■), Gd-DTPA-EOB (Ж), Gd-BOPTA (▲) and Mn-EDTA-EOB (●) by 10 mM Zn^{2+} plotted by ΔR_2 as a function of time 3 T and 293 K $\{\Delta R_2(t) = R_2(t) - R_2(0)\}$.

Cell viability assay and histology. The cytotoxic effects of Mn-EDTA-EOB on healthy human mammary epithelial cells (MCF-10A) and mouse normal liver cells (AML12) were evaluated by performing *in vitro* cell viability assay (CCK). The cells were incubated with Mn-EDTA-EOB, Gd-DTPA and Mn-DPDP complexes for 24 h. Here, Gd-DTPA was selected as a reference complex because Gd-DTPA has a well-established cell viability data. The viability percentage of the human mammary epithelial cells and mouse normal liver cells were retained above 82% and 88% for Mn-EDTA-EOB, whereas, clinically approved Mn-DPDP exhibit 63% and 79% cells viability, when incubated with increasing concentrations up to 50 μM (Figure S14). Although Mn-EDTA-EOB complex showed a decrease in cell viability at high concentration, the cell viability data demonstrate that Mn-EDTA-EOB has negligible toxicity for MCF-10A and AML12 cells at the dose required for MRI. In addition, to find out whether the injected Mn-EDTA-EOB causes any impairment *in vivo*, comprehensive histological study of the liver tissue section was carried out. H&E staining studies of the liver tissues did not show any apparent damage in cellular structures after 2 h injection of Mn-EDTA-EOB compared to the liver tissue without Mn-EDTA-EOB injection. No significant change in morphology was found up to 2 days of injection (see Figure S15).

***In vivo* biodistribution and pharmacokinetics.** The quantitative *in vivo* biodistribution of Mn-EDTA-EOB chelate was evaluated by an inductively coupled plasma (ICP) spectrophotometer (Figure 3). ICP data showed highest Mn^{2+} accumulation in the liver (around 26%) and

correspondingly in the intestine, indicating that Mn-EDTA-EOB was eliminated through the hepatobiliary route. For comparison, we selected Gd-DTPA-EOB complex, which is commercial liver-specific MR CA because Mn-EDTA-EOB showed strong possibility as potential liver-specific CA. Clinically used Gd-DTPA-EOB showed liver accumulation almost double within 30 min when compared with Mn-EDTA-EOB.[32] Besides the liver, the kidneys also exhibit comparatively high Mn accumulation, suggesting excretion via the renal pathway. The *in vivo* biodistribution data demonstrated that Mn-EDTA-EOB is excreted through both hepatobiliary and renal pathways. Although liver accumulation of Mn-EDTA-EOB is lower than that of Gd-DTPA-EOB, Mn-EDTA-EOB displays similar biodistribution pattern to Gd-DTPA-EOB.[30] It should be noted that, during biodistribution studies the urine and feces were excluded from bladder and intestine respectively. Also, the distribution half-life ($t_{d\ 1/2}$) and elimination half- life ($t_{e\ 1/2}$) of Mn-EDTA-EOB complex were 11 min and 2.3 h respectively (see Figure S16). In general, hepatobiliary excretion is relatively slower than renal clearance.

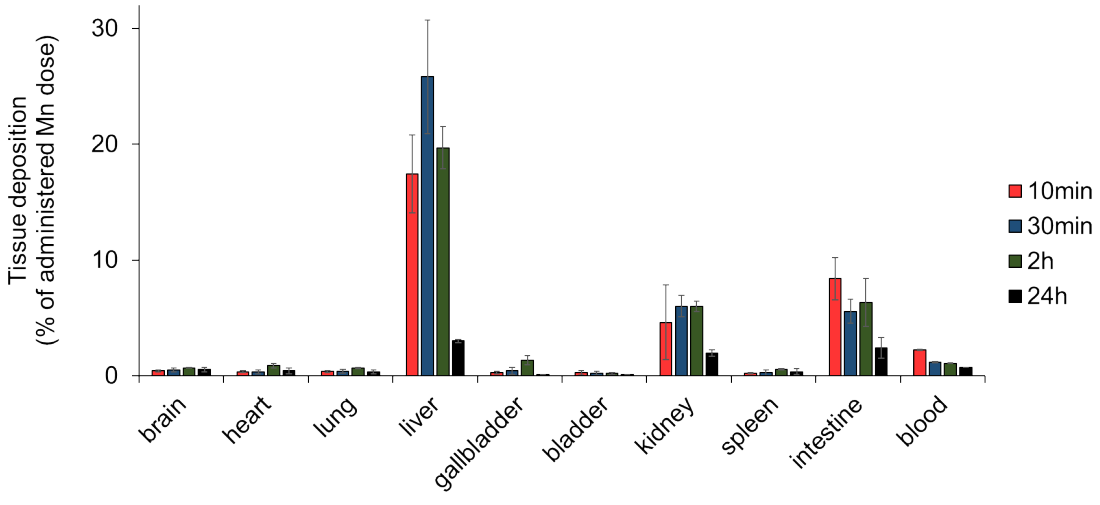

Figure 3. Biodistribution patterns of Mn-EDTA-EOB (0.05 mmol Mn/g) in normal ICR mice represented by Mn percentage in each tissue. Groups of mice (n = 4) were sacrificed at 10 min, 30 min, 2h and 24 h. Data are expressed as mean ± SD.

***In vivo* MRI of normal mice.** Six-week-old male ICR mice were used for *in vivo* T_1-weighted MRI after a bolus injection of Mn-EDTA-EOB through the tail vein (Figure 4). For comparison, we again selected Gd-DTPA-EOB and Gd-BOTPA which are commercial liver-specific MR CAs. The most distinctive MR feature of Mn-EDTA-EOB is that the contrast enhancement in the liver was similar to Gd-based liver CAs, such as Gd-DTPA-EOB and Gd-BOTPA, and gallbladder showed much higher enhancement after 60 min (Figure S17). Contrast-to-noise ratio (CNR) graphs of Mn-EDTA-EOB shows considerable signal increases in the kidney and liver, and correspondingly in the gallbladder. Together with the findings of biodistribution study, *in vivo* MR images confirm that Mn-EDTA-EOB is excreted through both the liver and kidneys. In the hepatobiliary pathway, Mn-EDTA-EOB is taken up by hepatocytes and eliminated via the biliary trees. Because of the paramagnetic properties of Mn^{2+}, Mn-EDTA-EOB causes T_1 enhancement of the liver and biliary trees. This dual elimination pattern of Mn-EDTA-EOB is similar to that of Gd-based liver-specific agents Gd-DTPA-EOB and Gd-BOTPA.[30,35]

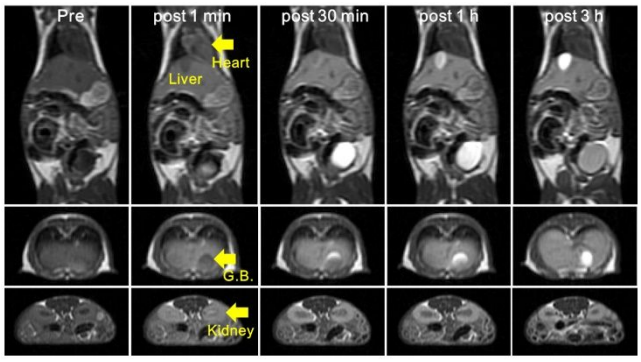

Figure 4. *In vivo* T_1-weighted spin echo (SE) MR images of normal ICR mice obtained after tail vein injection of Mn-EDTA-EOB (0.05 μmol Mn/g); G.B., gallbladder.

***In vivo* MRI characterization of liver tumor.** To investigate the clinical efficacy of Mn-EDTA-EOB chelate as a liver-specific CA, we performed *in vivo* MRI of liver tumor using an Huh-7 xenograft mouse tumor model after bolus injection of Mn-EDTA-EOB through the tail vein (Figure 5a). The liver tumor location and size were confirmed with T_2-weighted MR images before Mn-EDTA-EOB injection. Immediately after intravenous injection of Mn-EDTA-EOB, tumor tissues can be distinguished from the normal liver tissues owing to the greater signal intensity of normal liver than tumor tissues in T_1-weighted MR images (Figure 5a). Unlike extracellular fluid (ECF) agents, liver-specific hepatobiliary MRI CAs can be transported into normal hepatocytes.[36,37] The transportation of liver-specific MRI CAs into hepatocytes involves transport systems at the sinusoidal and canalicular membranes of hepatocytes.[38] The liver-specific CAs enter normal hepatocytes mostly through organic anion-transporting polypeptide transporters (OATPs).[39] However, OATPs are considerably reduced in HCC cells; therefore, HCC cells do not take up or excrete lipophilic agents and appear hypointense to the normal liver.[40,41]

In addition, CNR shows marked differences in the uptake of Mn-EDTA-EOB between normal hepatocytes and tumor cells, indicating a substantial difference in MR signal enhancement (Figure 5b). Moreover, color mapping images specify the normal (peach color) and tumor (brown color) liver regions after 90 min injection of Mn-EDTA-EOB when compared with pre-images (Figure 5c). Furthermore, we obtained an image histogram that shows the number of pixels at each different intensity value. Before injection of Mn-EDTA-EOB, the histogram showed insignificant signal intensity difference between normal and tumor regions. However,

after Mn-EDTA-EOB injection, the histogram showed a considerably higher signal intensity value of normal liver than that of tumor tissues, revealing the significantly enhanced normal hepatocytes (Figure 5d). Therefore, Mn-EDTA-EOB demonstrated remarkable clinical potential to detect liver tumors by distinguishing normal liver tissues from tumor tissues.

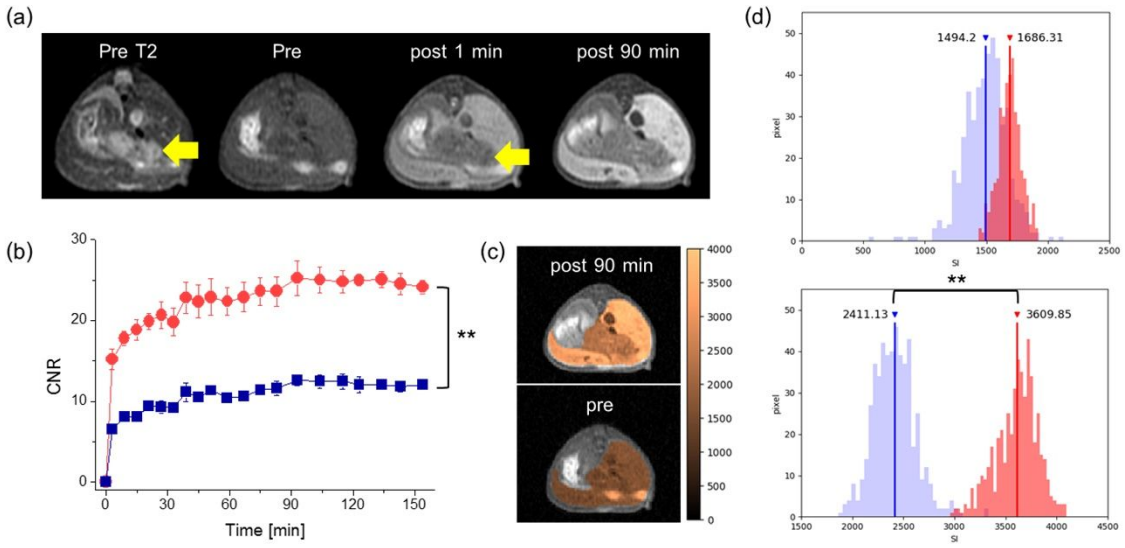

Figure 5. Axial T_2-weighted and T_1-weighted MR images of Huh-7 xenograft mice (a) before and after injection of Mn-EDTA-EOB (0.05 mmol Mn/kg). Yellow arrow indicates the liver tumor lesion. (b) CNR profiles of normal (red circles) and tumor (blue squares) liver tissue as a function of time. CNR was measured in axial T_1-weighted images. (c) Color mapping images of pre and post 90 min injection of Mn-EDTA-EOB. (d) Histogram of the pre and post 90 min axial images as signal intensity values. The signal intensity of tumor and normal liver regions was indicated by blue and red bars respectively. The vertical line of each distribution represents the average value. Statistical significance of the differences between the intensity of normal and tumor tissue was analyzed using the Mann-Whitney U test with SPSS software (**, $P \leq 0.01$; Z = -5.547 for b; Z = -27.419 for d).

Molecular docking simulation. The biodistribution pattern of Mn-EDTA-EOB complex is similar to that of Gd-DTPA-EOB and there is ample evidence that hepatic uptake of Gd-DTPA-

EOB is mediated by liver specific-uptake transport proteins such as OATPs and/or Na^+/taurocholate cotransporting polypeptide (NTCP).[42,43] We hypothesized that hepatic uptake of Mn-DTPA-EOB can be mediate by OATPs and/or NTCP due to the similar biodistribution pattern with Gd-DTPA-EOB and presence of EOB moiety in the compound structure. In many studies, molecular docking has been used to identify the effective binding sites and affinities.[44,45] Therefore, we performed computational modeling studies to identify the favorable transporter system for the uptake of Mn-EDTA-EOB complex into the liver.[45] Homology modeling approach was introduced to estimate the three-dimensional structures of OATPs and NTCP because of the lack of crystal structures of these proteins. Subsequently, protein-ligand docking simulations were performed.

Figure 6 shows the possible interactions between different transporter systems and Mn-EDTA-EOB. Among the different transporter systems, the results of docking simulation study demonstrated that OATP1b3 and OATP2b1 are more favorable than other transporter systems. Mn-EDTA-EOB forms several hydrogen bonds with OATP1b3 transporter, and K49 in OATP1b3 forms a salt bridge with Mn-EDTA-EOB complex. OATP2b1 forms hydrogen bonds with Mn-EDTA-EOB chelate, and K70 in OATP2b1 forms several salt bridges with Mn complex. F156 of OATP2b1 also forms pi-pi stacking with the phenyl ring of Mn complex. The docking scores, which were calculated using Schrödinger suite software, between Mn-EDTA-EOB and transport proteins were -11.58 kcal/mol for OATP1b3 and -11.12 kcal/mol for OATP2b1 (Table 2). However, OATP1b1 and NTCP only form hydrogen bonds and/or salt bridges with Mn-EDTA-EOB complex. The docking score between Mn-EDTA-EOB and OATP1b1 was -9.36 kcal/mol and that between Mn-EDTA-EOB and NTCP was -10.67 kcal/mol

(Table 2). Therefore, the docking simulation studies demonstrate that Mn-EDTA-EOB uses OATP1b3 and OATP2b1 as the major gateway for hepatic uptake.

For comparison, computational docking studies of Gd-DTPA-EOB, EDTA-EOB and Mn-EDTA also performed and are shown in Table 2 and Figure S18-S20. Mn-EDTA-EOB shows much higher interaction with different transporters, when compared with EDTA-EOB and Mn-EDTA. One of the major modes of transport is the OATP1 series. Although 1b1 and 1b3 of OATP are expressed in normal liver tissue, the expression of OATP1b1 and OATP1b3 decreases in liver tumors according to the degree of differentiation of tissues.[46] This pattern is in good agreement with in vivo MR image (Figure 5).

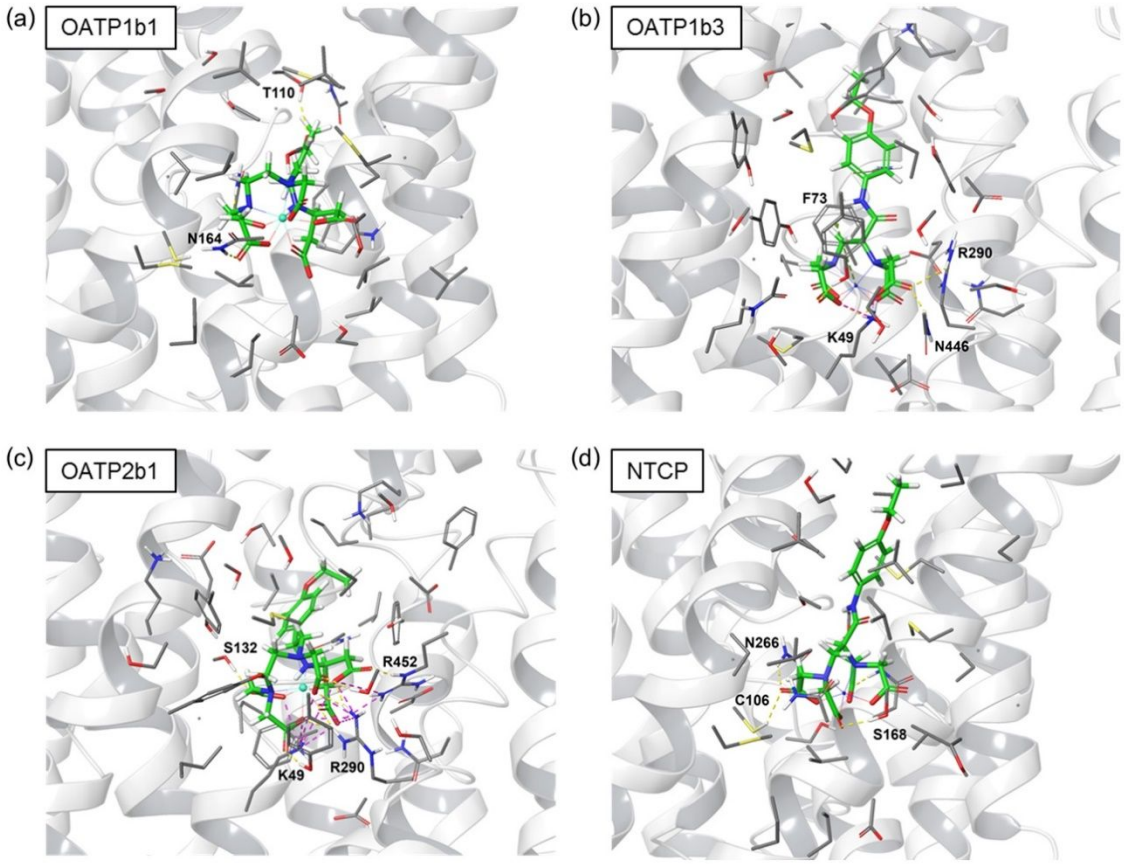

Figure 6. Schematic representations of variable interactions between Mn-EDTA-EOB and (a) OATP1b1, (b) OATP1b3, (c) OATP2b1 (PDB ID: 2GFP, gray), and (d) NTCP (PDB ID: 3ZUY, gray). These images show the amino acids within 5 Å around the Mn-EDTA-EOB. The yellow line represents hydrogen bond, the pink line represents salt bridge, the green represents pi-cation interaction, and the cyan represents pi-pi stacking interaction.

Table 2. Docking scores of the Mn-EDTA-EOB, EDTA-EOB, Mn-EDTA and the commercial agent Gd-DTPA-EOB with liver specific-organic anion transporter proteins.

	OATP1b3	**OATP1b1**	**OATP2b1**	**NTCP**
Mn-EDTA-EOB	-11.58	-9.36	-11.12	-10.67
Gd-DTPA-EOB	-11.54	-13.25	-12.38	-12.78
EDTA-EOB	-9.24	-8.99	-9.83	-13.25
Mn-EDTA	-8.75	-9.83	-8.07	-9.61

(kcal/mol)

CONCLUSION

In the present study, we synthesized a novel Mn-EDTA complex with high kinetic inertness by combining a lipophilic EOB moiety and studied its possible diagnostic efficacy as a liver-specific MRI CA. It showed higher r_1 relaxivity (2.3 mM^{-1} s^{-1}) than clinically approved Mn-DPDP (1.6 mM^{-1} s^{-1}) at 1.5 T. The kinetic inertness of Mn-EDTA-EOB chelate is much higher than that of Gd-based liver-specific MRI CAs (Gd-DTPA-EOB and Gd-BOPTA) and previously reported Mn-based liver-specific CAs (Mn-DPDP and Mn-EDTA-BTA). The biodistribution pattern and *in vivo* MR images showed that Mn-EDTA-EOB is excreted through both hepatobiliary and renal pathways. The molecular docking simulation study suggests that Mn-EDTA-EOB might use OATP1b3 and OATP2b1 transport systems as the major gateway for hepatic uptake. Finally, in a liver tumor model, Mn-EDTA-EOB demonstrated significant

improvement in tumor detection and characterization, suggesting that this new chelate can be a prominent MRI agent for liver cancer, particularly in patients with compromised renal function.

EXPERIMANTAL PROCEDURES

General Remarks. All reagents were purchased from Tokyo Chemical Industry (Tokyo, Japan), Sigma-Aldrich (St. Louis, MO, USA), and/or Alfa-Aesar (Ward Hill, MA, USA) and used without additional purifications. Solvents were dried and purified using standard methods. Deionized (DI) water was used for all experimental procedures.^{1}H NMR spectrums were measured on a 500 MHz (Bruker Advance) at the Kyungpook National University (KNU). Tetramethyl silane (TMS) was used as an interior standard for chemical shifts. Elemental analyses (EA) were accomplished in KNU. The detailed methods for High-resolution fast atom bombardment mass spectrums (HR-FAB-MS) and High-pressure liquid chromatography (HPLC) are given elsewhere (See reference 26). Electrospray ionization mass spectrometry (ESI-MS) was obtained by using a Q Exactive quadrupole Orbitrap mass spectrometer (Thermo Fisher Scientific Inc., Rockford, IL, USA) at department of chemistry, KNU. Methods used for purity tests were as follows: Eluent A, 10 mM ammonium acetate in water; B, 10 mM ammonium acetate in ACN; gradient, 5% B to 70% B in 25 min, 70% B to 100% B in 5 min, 100% B in 10 min; flow rate 12 mL/min. Purity of the synthesized compounds were confirmed by elemental analysis or a reverse-phase HPLC with UV−vis detection at 254 nm and purity of the final complex was 95% or higher. No unexpected or unusual high safety hazards were encountered during experimental procedures.

Synthesis and Characterization. 2, 3-Bis-*tert*-butoxycarbonylaminopropionic Acid (1). Title compound was synthesized according to a published literature with slight modifications.[29]

[2-*tert*-Butoxycarbonylamino-2-(4-ethoxy-phenylcarbamoyl)-ethyl]-carbamic acid *tert*-butyl ester (2). Compound **1** (2 g, 6.57 mmol), N, N-diisopropylethylamine **(**1.6 mL, 13.15 mmol**)**, HOBt (1.25 g, 8.21 mmol) and HBTU (3.73g, 9.85 mmol) were dissolved in DMF. 4-Ethoxyaniline (1.13g, 8.21 mmol) was slowly added and stirred for 18 h at room temperature. Resulting mixture was diluted with DI water and extracted with ethyl acetate (3×20 mL). Organic layer was washed with brine and dried over $MgSO_4$. Crude compound was recrystallized with dichloromethane and pure product was collected as a white solid. Yield: 1.9 g (69%). ^{1}H NMR (MeOD-d_4): δ = 9.77 (*s*, 1H, NH), 7.47 (*s*, 2H, NH) 6.86−6.79 (*dd*, 4H, CH), 4.41 (*t*, 1H, CH), 3.97 (*dd*, 2H, CH_2), 1.39 (*s*, 18H, CH_3), 1.32 (*t*, 3H, CH_3), 1.29 (*d*, 2H, CH_2). Anal. Calcd for $C_{21}H_{33}N_3O_6$: C, 59.56; H, 7.85; N, 9.92. Found: C, 59.30; H, 7.95; N, 9.90. HR-FAB-MS (m/z) for $C_{21}H_{33}N_3O_6$: calcd, 423.2369 $[M]^+$ and 424.2448 $[M + H]^+$; found, 423.2372 $[M]^+$ and 424.2445 $[M + H]^+$.

2, 3-Diamino-N-(4-ethoxy-phenyl)-propionamide (3). Trifluoracetic acid (TFA) was carefully added into the solution of compound **2** (1.5 g, 3.54 mmol) in dichloromethane (CH_2Cl_2) at 0 °C. For 18 h, the solution was stirred to consume starting materials. Solvent was removed and ethyl ether was added to obtained precipitate. Solid appears was filtered and washed with ethyl ether several times. After vacuum dried pure product was collected as pale-yellow solid. Yield: 0.75 g (95%). ^{1}H NMR (MeOD-d_4): δ = 7.54 (*d*, 2H, CH) 6.89 (*d*, 2H, CH), 4.32 (*t*, 1H, CH), 4.02 (*dd*, 2H, CH_2), 1.37 (*t*, 3H, CH_3), 1.18 (*d*, 2H, CH_2). Anal. Calcd for $C_{11}H_{19}N_3O_3 \cdot 4CF_3CO_2H$: C, 32.72; H, 3.32; N, 6.03. Found: C, 33.06; H, 3.29; N, 5.93. HR-FAB-MS (m/z) for $C_{11}H_{18}N_3O_2$: calcd, 224.1399 $[M + H]^+$; found, 224.1402 $[M + H]^+$.

{[2-(Bis-*tert*-butoxycarbonylmethyl-amino)-1-(4-ethoxy-phenylcarbamoyl)-ethyl]-*tert*-butoxycarbonylmethyl-amino}-acetic acid *tert*-butyl ester (4). Compound **3** (2 g, 8.92 mmol),

diisopropylethylamine (6.92 mL, 53.57 mmol) and potassium iodide (2.96 g, 17.84 mmol) were dissolved in DMF. *tert*-Butyl bromoacetate (10.43 mL, 53.57 mmol) was added dropwise and heated to 110 °C for 4 h. Solvent was removed and residue was partitioned between ethyl acetate and 10% $NaHCO_3$ solution. Organic layer was collected, washed with brine and dried over Na_2SO_4. After evaporation crude product was collected and purified by column chromatography (silica, hexanes/EtOAc, 9:1). Yield: 5.4 g (88%). ^{1}H NMR (DMSO-d_6): δ = 10.23 (*s*, 1H, NH), 7.47 (*d*, 2H, CH) 6.88 (*d*, 2H, CH), 3.98 (*dd*, 2H, CH_2), 3.61 (*t*, 1H, CH), 3.57-3.40 (*m*, 8H, CH_2), 3.18-2.89 (*dd*, 2H, CH_2), 1.40 (*s*, 36H, CH_3), 1.30 (*t*, 3H, CH_3). Anal. Calcd for $C_{35}H_{57}N_3O_{10}\cdot 2H_2O$: C, 58.72; H, 8.59; N, 5.87. Found: C, 58.35; H, 8.73; N, 5.83. HR-FAB-MS (m/z) for $C_{35}H_{58}N_3O_{10}$: calcd, 680.4122 $[M + H]^+$; found, 680.4127 $[M + H]^+$.

{[2-(Bis-carboxymethyl-amino)-1-(4-ethoxy-phenylcarbamoyl)-ethyl]-carboxymethyl amino}-acetic acid (L). Compound **4** (1.5 g, 2.20 mmol) was dissolved in a mixture of trifluoracetic acid and dichloromethane using ice bath. Resulting solution was stirred until starting materials was disappeared. Ether was added to obtained precipitate after removing solvent. Then filttred and dried to get pure product as off-white solid. Yield: 0.96 g (96%). ^{1}H NMR (MeOD-d_4): δ = 7.48 (*d*, 2H, CH) 6.87 (*d*, 2H, CH), 4.09 (*d*, 4H, CH_2), 3.98 (*dd*, 2H, CH_2), 3. 57-3.56 (*m*, 6H, CH_2), 1.46 (*t*, 3H, CH_3). Anal. Calcd for $C_{19}H_{25}N_3O_{10}\cdot 1/2CF_3CO_2H$: C, 47.20; H, 5.07; N, 8.31. Found: C, 46.85; H, 5.15; N, 8.28. HR-FAB-MS (m/z) for $C_{19}H_{26}N_3O_{10}$: calcd, 456.1618 $[M + H]^+$; found, 456.1621 $[M + H]^+$.

[Mn (EDTA-EOB) (H_2O)]$^{2-}$. Ligand L (0.6 g, 1.3 mmol) was dissolved in DI water and pH of the solution was adjusted to 6.5 by carefully addition of NaOH (1M). $MnCl_2\cdot 4H_2O$ (0.26 g, 1.3 mmol) was slowly added and resulting solution was stirred for three days at RT. During this time pH of solution was readjusted for several times. After lyophilization crude product was collected

as solid and extra purification was performed by preparative HPLC and purity was also confirmed (see Figure S10). Yield: 0.38g (58%). ESI-MS (m/z) for $C_{19}H_{22}MnN_3O_{10}$: calcd, 507.0686 $[M+H]^+$; found, 507.0682 $[M+H]^+$.

Relaxivity. Relaxivities were measured with 1.5 T GE unit (GE Healthcare). T_1 measurements were carried out at 35 different inversion times (TIs) range between 50 and 1750 ms using an inversion recovery technique. In case of T_2, the CPMG (Carr−Purcell−Meiboon−Gill) pulse sequence was used at 34 different echo times (TEs) range from 10 to 1900 ms. The nonlinear least-squares fit of the average pixel were used to estimate T_1 and T_2 relaxation. Then, r_1 and r_2 relaxivities were computed by the linear fit of T_1 and T_2 relaxation time for each concentration (0.0625, 0.125, 0.25, 0.5, and 1 mM).

Octanol-Water Partition Coefficients. This experiment was accomplished according to a published literature method.[47] 1 mg sample of Mn-EDTA-EOB complex was dissolved in 2 mL of water and 1-octanol mixture (1:1 v/v). Resulting mixture was shaken for a second, then the vial was gently mixed on a rotator for 48 h. The mixture was then placed on the desk and allowed to be divided into two layers for 24 h at room temperature. Mn concentrations of each layer were measured by inductively coupled plasma mass spectrometry (ICP-MS). Octanol-water partition coefficients were computed using the equation log P = $\log(C_o/C_w)$, where log P is the common logarithm of the partition coefficient, C_o and Cw are the concentration of Mn in the 1-octanol layer and water layer, respectively.

Transmetallation Kinetics. This experiment was directed according to the published procedure with trivial modifications.[28,29] 50 μL of a 100 mM MES [2-(N-morpholino) ethane sulfonic acid] buffered solution (pH 6) of $ZnCl_2$ was added to a 450 μL of 1.25 mM buffered solution of Mn-EDTA-EOB complex. The final concentration we use for this experiment was 1 mM solution of

Mn-EDTA-EOB complex and 10 mM $ZnCl_2$. The mixture was shaken for a while then instantly used for measuring solvent T_2. For comparison purpose Mn-EDTA, Mn-EDTA-BTA, Mn-DPDP (Teslascan), Gd-DTPA-EOB (Primovist) and Gd-BOPTA (MultiHance) were also studied. The measurements were conducted on a 3 T system (Magnetom Tim Trio, Siemens, Germany) for 72 hours at room temperature. The diagram was plotted using the equation $\{\Delta R_2(t) = R_2(t) - R_2(0)\}$ as a function of time. N=3 for each complex and average value was used for calculation.

Determination of Binding Constants. The binding affinity of Mn-EDTA-EOB chelate with HSA was measured by method in literatures.[33,48] The nonlinear rise of the ^1H relaxation rates was fitted using eq 1, where N is the number of independent interaction sites (N was set to 1), p^0 is the concentration of the HSA, s^0 is the paramagnetic complex concentration, and r_1^c and r_1^f are the relaxivities of the complex HSA-contrast agent and of the free contrast agent, respectively.

$$R_1^{p^{obs}} = 1000 \times \left\{ \left(r_1^f \times s^0\right) + \frac{1}{2}\left(r_1^c - r_1^f\right) \left(\left(N \times p^0\right) + s^0 + K_a^{-1} - \sqrt{\left(\left(N \times p^0\right) + s^0 + K_a^{-1}\right)^2 - 4 \times N \times s^0 \times p^0} \right) \right\} \quad (1)$$

Kinetic stability in various pH regions. The stability was given in the evolution of the water proton relaxation rate (R_1) for Mn-EDTA-EOB in various buffer solution at different pH ranges (pH: 1,3,5,7,9 and 11) as a function of time.[49] The measurements were performed on a 3 T whole body system (Magnetom Tim Trio, Simens, Germany) at room temperature for 12 days.

Cell Culture. The culture medium contained of 1% (v/v) penicillin−streptomycin, 10% (v/v) fetal bovine serum (FBS), and Dulbecco's Modified Eagle Medium/Nutrient Mixture F-12 (DMEM/F12, Gibco Invitrogen, Carlsbad, CA).

Cell preparation for MR imaging. Mouse normal liver cells (AML12) and human mammary epithelial cells (MCF-10A) were plated at a density of 2 X 10^5 in 35 mm dishes. The DMEM growth medium was removed, and the cells were incubated with Mn-EDTA-EOB (0, 5 and 50 μM) in DMEM/F-12 growth media for 24 h. The cells were washed with phosphate buffered saline (PBS) and harvested. Media with trypsin-EDTA was removed and cells were resuspended with DMEM/F-12 growth media.

Cell Viability Assay. Human mammary epithelial cell line (MCF-10A) and mouse normal liver cell line (AML12) were purchased from ATCC (Manassas, Virginia) and plated in 96-well plates at a density of 1×10^4. The DMEM/F-12 growth medium were removed and Mn-EDTA-EOB, Mn-DPDP and/or Gd-DTPA chelates were incubated with cells in DMEM/F-12 serum-reduced medium for 24 h. The cell viability of Mn-DPDP with various Mn^{2+} concentration was provided as control. Using the CCK-8 kit (Dojindo, Sunnyvale, CA), cell viability was computed according to the manufacturer's protocol. Briefly, to each well CCK-8 solution (10 μL) was added then the samples were incubated for 2 h and absorbance of samples were detected at 450 nm.

Pharmacokinetic study. Pharmacokinetic studies were conducted by following previously published procedure with slight modification.[50] Blood plasma was assessed on 5-week-old male BALB/c mice (28-30 g). Blood samples (total 60 μL) were pooled from three mice (20 μL from each mice) for one group and four group were used for study. Blood samples were collected from the tail vein before injection and at 10, 30 min, 1, 3, 6, 9 and 12 hour after injection of Mn-

EDTA-EOB at a dose of 0.05 mmol/kg. The collected samples were immediatly mixed with heparin solution and centrifuged at 5000 rpm at 4 ^{o}C for 10 min to obtain plasma. The plasma were treated with 70 % nitric acid (HNO_3) and 30% hydrogen peroxide (H_2O_2) at 180 °C for 3 h. The manganese concentration of the treated sample was measured by an inductively coupled plasma spectrophotometer (NexION 300X, PerkinElmer, USA). The recognition limit of this process is 1 ppb. Blood plasma pharmacokinetics were estimated by plotting the Mn concentration as a function of time and fitting the decay to a biexponential function using MATLAB curve fitting tool. The distribution and elimination half-lives ($t_{d\ 1/2}$, $t_{e\ 1/2}$) were estimated, respectively.

H&E staining. For histological evaluation, portions of liver collected on 2 hour and 2 day after injection of Mn-EDTA-EOB (0.05 mmol/kg) were fixed in 4 % paraformaldehyde buffer solution for one and a half day and then embedded in paraffin blocks. Tissue sections 3 μm thick were stained with hematoxylin and eosin (H&E).[51]

***In vitro* MR Imaging.** In vitro MR images were obtained using a 3 T MR scanner (GE Healthcare, Milwaukee, WI, USA). The imaging parameters for T_1-weighted image were as follows: repetition time (TR) = 300 ms; echo time (TE) = 9 ms; 26 mm field of view (FOV); 192 X 192 matrix size; 13.0 mm slice thickness; number of acquisition (NEX) = 15.

***In Vivo* MR Imaging.** All animal trials were permitted by Kyungpook National University Animal Care Committee and tests were performed in agreement with their rules. For MRI studies, all animal protocols were same as the protocols given previously (See reference 29). MR measurements were performed with a 1.5 T MRI (GE healthcare) and imaging protocols including sequence parameters were same as the methods given previously (See reference 29). The color-mapped images at maximum enhanced time (90 min) and the histograms of the normal

and tumor liver region were obtained by using Python 3.6. All scripts were composed by using the python library Matplotlib.

Liver Tumor Model. An orthotopic model of liver cancer was used by the approval of the Institutional Animal Care and Committee of Daegu-Gyeongbuk Medical Innovation Foundation (DGMIF). Five-week-old male nude mice (BALB/c nu/nu) were obtained from Central Lab Animal Inc. (Seoul, Korea). The Huh-7 cell line was gained from PerkinElmer Inc. and cells (5×10^6 cells in 50 μL of DMEM) were inoculated in the liver of the mice.

Image Analysis. The program Image J (NIH, USA) was used for measurement of signal intensity values for specific regions of interest (ROI). The CNR (contrast-to-noise ratio) was estimated by means of eq 2, where SNR is the signal-to-noise ratio.

$$CNR = SNR_{post} - SNR_{pre} \quad (2)$$

Biodistribution study. After intravenously injection of Mn-EDTA-EOB (0.05 mmol/kg) to six-week-old normal male mice (ICR; 25-30 g) through tail veins, the mice were anesthetized and sacrificed at 4 different time points (10 min, 30 min, 2 h and 24 h after injection). Blood and various organs were collected and treated with 70 % nitric acid (HNO_3) and 30% hydrogen peroxide (H_2O_2) at 180 °C for 3 h. The manganese concentration of the treated sample was measured by an inductively coupled plasma spectrophotometer (ICP-spectrophotometer, Optima 7300DV, PerkinElmer, USA). The recognition limit of this process is 0.01 ppm.[52]

Statistical analysis. Data are presented as mean ± standard error if there is no other description. Statistical analysis was performed using the Mann-Whitney U test with SPSS software. Curve fits were done using MATLAB curve fitting tool.

Molecular Modeling. Three-dimensional structures of OATP1B1, OATP1B3, OATP2B1 and NTCP were predicted using homology modeling method. Crystal structure of the multidrug transporter EmrD (PDB ID: 2GFP) and crystal Structure of a bacterial homologue of the bile acid sodium symporter Asbt (PDB ID: 3ZUY) were selected as template structures for OATPs and NTCP homology modeling, respectively. Three-dimensional structures of the four proteins were constructed by Prime [55] homology modeling application. After that, Prime [55] structure optimization tool was performed to optimize the structures under implicit solvent and membrane environments. Protein-ligand docking calculations were performed using Glide (Grid-based Ligand Docking with Energetics) [56] of the Schrödinger suite. Glide searches for favorable interactions between small molecules and a receptor protein. In Glide, molecules were described using OPLS 2005 force filed and the SP (standard precision) mode of Glide was used allowing flexible ligand sampling. Delta G scores of the docked ligands were calculated by empirical scoring function called Glide score.

AUTHOR INFORMATION

Corresponding Author

*Y.C.: E-mail, ychang@knu.ac.kr. Phone, (+)82-53-420-5471.

ORCID

Yongmin Chang: 0000-0002-0585-8714

Md. Kamrul Islam: 0000-0001-8411-4766

Author Contributions

† Md. K.I. and S.K. contributed equally to the work. The manuscript was written through contributions of all authors. All authors have given approval to the final version of the manuscript.

Notes

The authors declare no competing financial interest**.**

ACKNOWLEDGMENTS

This work was supported by the Basic Science Research Program (Grant 2017R1A2B3003214) through the National Research Foundation of Korea funded by the Ministry of Science and ICT. The authors are further thankful to Dr. Thamina Acter for her help with the ESI-MS analysis.

Supporting information

The Supporting Information is available free of charge on the ACS Publications website at DOI: bc-2018-00560v

Chemical compound characterizations data (^{1}H NMR, HR-FAB-MS, ESI-MS and HPLC spectra), cell viability assay, H&E staining, pH stability, T_1-weighted MRI images, CNR profiles and computational modeling studies. (PDF)

ABBREVIATIONS USED

EDTA, ethylenediaminetetraacetic acid; EOB, ethoxybenzyl ; MRI, magnetic resonance imaging; Mn-DPDP, mangafodipir trisodium; NSF, nephrogenic systemic fibrosis; CA, contrast agent; Gd-DTPA, gadopentetic acid; ICR, Institute of Cancer Research; CNR, contrast to noise

ratio; Gd-DTPA-EOB, gadoxetic acid; Gd-BOPTA, gadobenic acid; rt, room temperature; HPLC, high performance liquid chromatography; MES, (2-(N-morpholino)- ethanesulfonic acid); Mn-EDTA, ethylenediaminetetraacetic acid manganese disodium salt hydrate; GB, gallbladder; OATP, organic anion transporter polypeptide; MRP, multidrug resistance protein; ECF, extracellular fluid; TI, inversion time; CPMG, Carr−Purcell−Meiboon−Gill pulse sequence; TE, echo time; TR, repetition time; SE, spin echo; FSE, fast spin echo; FOV, field of view; NEX, number of acquisition; HCC, hepatocellular carcinoma; ROI, regions of interest; ICP, inductively coupled plasma; DMEM, Dulbecco's modified Eagle medium; RPMI, Roswell Park Memorial Institute; FBS, fetal bovine serum; HSA, human serum albumin; PBS, phosphate buffered saline; HBSS, Hank's balanced salt solution; IVIS, *in vivo* imaging instruments; RIPA, radioimmunoprecipitation assay; CCK-8, cell counting kit-8; PDB, protein data bank; NTCP, sodium/taurocholate cotransporting polypeptide.

REFERENCES

(1) Schraml, C.; Kaufmann, S.; Rempp, H.; Syha, R.; Ketelsen, D.; Notohamiprodjo, M.; Nikolaou, K. (2015) Imaging of HCC-Current State of the Art. *Diagnostics 5*, 513−545.

(2) American Cancer Society. (2018) Cancer Statistics Center. http://cancerstatisticscenter.cancer.org. 2018.

(3) Llovet, J. M.; Fuster, J.; Bruix, J. (1999) Intention-to-treat analysis of surgical treatment for early hepatocellular carcinoma: Resection versus transplantation. *Hepatology 30*, 1434–1440.

(4**)** Caravan, P., Ellison, J. J., Thomas, J., McMurry, and Lauffer, R. B. (1999) Gadolinium (III) Chelates as MRI Contrast Agents: Structure, Dynamics, and Applications**.** *Chem. Rev. 99*, 2293–2352.

(5**)** Kim, H. K., Lee, G. H., and Chang, Y. (2018) Gadolinium as an MRI contrast agent. *Future Med. Chem. 10* (6), 639–661.

(6) Geraldes, C., and Laurent, S. (2009) Classification and basic properties of contrast agents for magnetic resonance imaging. *Contrast Media Mol. Imaging 4*, 1–23.

(7) Grobner, T. (2006) Gadolinium a specific trigger for the development of nephrogenic fibrosing dermopathy and nephrogenic systemic fibrosis? *Nephrol. Dial. Transplant 21*, 1104–1108.

(8) Rodriguez, P. J., Lai, S., Ehst, B. D., Fine, D. M., and Bluemke, D. A. (2009) Nephrogenic Systemic Fibrosis: Incidence, Associations, and Effect of Risk Factor Assessment−Report of 33 Cases. *Radiology 250*, 371–377.

(9) Kanda, T., Fukusato, T., Matsuda, M., Toyoda, K., Oba, H., Kotoku, J., Haruyama, T., Kitajima, K., and Furui, S. (2015) Gadolinium-based contrast agent accumulates in the brain even in subjects without severe renal dysfunction: evaluation of autopsy brain specimens with inductively coupled plasma mass spectroscopy. *Radiology 276*, 228–232.

(10) McDonald, R. J., McDonald, J. S., Kallmes, D. F., Jentoft, M. E., Murray, D. L., Thielen, K. R., WIlliamson, E. E., and Eckel, L. J. (2015) Intracranial Gadolinium Deposition after Contrast-enhanced MR Imaging. *Radiology 275*, 772–782.

(11) Kanal, E., and Tweedle, M. F. (2015) Residual or Retained Gadolinium: Practical Implications for Radiologists and Our Patients. *Radiology 275*, 630–634.

(12) Drahos, B., Lukes, I., and Toth, E. (2012) Manganese (II) complexes as potential contrast agents for MRI. *Eur. J. Inorg. Chem. 2012* (12), 1975–1986.

(13) Kueny-Stotz, M., Garofalo, A., and Felder-Flesch, D. (2012) Manganese enhanced MRI contrast agents: from small chelates to nanosized hybrids. *Eur. J. Inorg. Chem. 2012* (12), 1987–2005.

(14) Yu, M., Ambrose, S. L., Whaley, Z. L., Fan, S., Gorden, J. D., Beyers, R. J., Schwartz, D. D., and Goldsmith, C. R. A (2014) Mononuclear Manganese (II) Complex Demonstrates a Strategy to Simultaneously Image and Treat Oxidative Stress. *J. Am. Chem. Soc. 136*, 12836−12839.

(15) Yu, M., Ward, M. B., Franke, A., Ambrose, S. L., Whaley, Z. L., Bradford, T. M., Gorden, J. D., Beyers, R. J., Schwartz, D. D., and Goldsmith, C. R., et al. (2017) Adding a Second Quinol to a Redox-Responsive MRI Contrast Agent Improves Its Relaxivity Response to H_2O_2. *Inorg. Chem. 56*, 2812−2826.

(16) Su, H., Wu, C., Zhu, J., Miao, T., Wang, D., Xia, C., Zhao, X., Gong, Q., Song, B., and Ai, H. (2012) Rigid Mn (II) chelate as efficient MRI contrast agent for vascular imaging. *Dalton Trans. 41*, 14480–14483.

(17) Barandov, A., Bartelle, B. B., Gonzalez, B. A., White, W. L., Lippard, S. J., and Jasanoff, A. (2016) Membrane-Permeable Mn (III) Complexes for Molecular Magnetic Resonance Imaging of Intracellular Targets. *J. Am. Chem. Soc.*, *138* (17), 5483–5486.

(18) Bedika, P., Anant, P. B., and Chandan, M. (2015) A water-soluble and water-coordinated Mn (II) complex: synthesis, characterization and phantom MRI image study. *Dalton Trans. 44*, 12990–12994.

(19) Forgacs, A., Figueroa, M. R., Barriada, J. L., Gomez, D. E., Blas, A. D., Blas, T. R., Botta, M., and Iglesias, C. P. (2015) Mono ‑, Bi ‑, and Trinuclear Bis-Hydrated Mn^{2+} Complexes as Potential MRI Contrast Agents. *Inorg. Chem. 54*, 9576−9587.

(20) Vanasschen, C., Molnar, E., Tircso, G., Kalman, F. K., Toth, E., Brandt, M., Coenen, H. H., and Neumaier, B. (2017) Novel CDTA-based, Bifunctional Chelators for Stable and Inert Mn (II) Complexation: Synthesis and Physicochemical Characterization. *Inorg. Chem. 56*, 7746−7760.

(21) Forgacs, A., Paradela, R. P., Figueroa, M. R., Valencia, L., Gomez, D. E., Botta, M., and Iglesias, C. P. (2017) Developing the family of picolinate ligands for Mn^{2+} complexation. *Dalton Trans. 46*, 1546–1558.

(22) Aschner, M., Guilarte, T. R., Schneider, J. S., and Zheng, W. (2007) Manganese: Recent advances in understanding its transport and neurotoxicity. *Toxicol. Appl. Pharmacol. 221*, 131–147.

(23) Pan, D., Schmieder, A. H., Wickline, S. A., and Lanza, G. M. (2011) Manganese-based MRI contrast agents: past, present, and future. *Tetrahedron 67*, 8431–8444.

(24) Bock, N. A., and Silva, A. C. (2007) Manganese: a unique neuroimaging contrast agent. *Future Neurol. 2*, 297–305.

(25) Gallez, B., Bacic, G., and Swartz, H. M. (1996) Evidence for the Dissociation of the Hepatobiliary MRI Contrast Agent Mn-DPDP. *Magn. Reson. Med. 35*(1),14–19.

(26) Seale, M. K., Catalano, O. A., Saini, S., Hahn, P. F., and Sahani, D. V. (2009) Hepatobiliary-specific MR Contrast Agents: Role in Imaging the Liver and Biliary Tree. *Radiographics 29*, 1725–1748.

(27) Mingqian, T., Zhen, Y., Eun, K. J., Xueming, W., Dennis L. P., and Zheng, R.L. (2011) Synthesis and Evaluation of Nanoglobular Macrocyclic Mn (II) Chelate Conjugates as Non-Gadolinium (III) MRI Contrast Agents. *Bioconjugate Chem. 22*, 931–937.

(28) Gale, E. M., Atanasova, I. P., Blasi, F., Ay, I., and Caravan, P. (2015) A manganese alternative to gadolinium for MRI contrast. *J. Am. Chem. Soc. 137*, 15548–15557.

(29) Islam, M. K., Kim, S., Kim, H. K., Park, S., Lee, G. H., Kang, H. J., Jung, J. C., Park, J. S., Kim, T. J., and Chang, Y. (2017) Manganese Complex of Ethylenediaminetetraacetic Acid (EDTA)− Benzothiazole Aniline (BTA) Conjugate as a Potential Liver-Targeting MRI Contrast Agent. *J. Med. Chem. 60*, 2993–3001.

(30) Hamm, B., Staks, T., Andreas M., Muhler, A., Bollow, M., Taupitz, M., Frenzel, T., Wolf, K. J., Weinmann, H. J., and Lange, L. (1995) Phase I clinical evaluation of Gd-EOB-DTPA as a hepatobiliary MR contrast agent: safety, pharmacokinetics, and MR imaging. *Radiology 195* (3)**,** 785–792.

(31) Troughton, J. S., Greenfield, M. T., Greenwood, J. M., Dumas, S., Wiethoff, A. J., Wang, J., Spiller, M., McMurry, T. J., and Caravan, P. (2004) Synthesis and evaluation of a high relaxivity manganese (II)-based MRI contrast agent. *Inorg. Chem. 43*, 6313–6323.

(32) Baek, A. R., Kim, H. K., Park, S., Lee, G. H., Kang, H. J., Jung, J. C., Park, J. S., Ryeom, H. K., Kim, T. J., and Chang, Y. (2017) Gadolinium Complex of 1,4,7,10-Tetraazacyclododecane-1,4,7- trisacetic Acid (DO3A) −Ethoxybenzyl (EOB) Conjugate as a New Macrocyclic Hepatobiliary MRI Contrast Agent. *J. Med. Chem. 60*, 4861−4868.

(33) Muller, R. N., Raduchel, B., Laurent, S., Platzek, J., Pierart, C., Mareski, P., and Vander Elst, L. (1999) Physicochemical characterization of MS-325, a new gadolinium complex, by multinuclear relaxometry. *Eur. J. Inorg. Chem. 1999* (11), 1949−1955.

(34) Laurent, S., Elst, L. V., Copoix, F., Muller, R. N. (2001) Stability of MRI Paramagnetic Contrast Media A Proton Relaxometric Protocol for Transmetallation Assessment. *Invest. Radiol. 36* (2), 115−122.

(35) Pavone, P., Patrizio, G., Buoni, C., Tettamanti, E., Passariello, R., Musu, C., Tirone, P., and Felder, E. (1990) Comparison of Gd-BOPTA with Gd-DTPA in MR imaging of rat liver. *Radiology 176* (1), 61−64.

(36) Narita, M., Hatano, E., Arizono, S., Hayashino, M. A., Isoda, H., Kitamura, K., Taura, K., Yasuchika, K., Ikai, I., Uemoto, S., et al. (2009) Expression of OATP1B3 determines uptake of Gd-EOB-DTPA in hepatocellular carcinoma. *J Gastroenterol 44*, 793−798.

(37) Kiryu, S., Inoue, Y., Watanabe, M., Izawa, K., Shimada, M., Tojo, A., Yoshikawa, K., and Ohtomo, K. (2009) Evaluation of gadoxetate disodium as a contrast agent for mouse liver imaging: comparison with gadobenate dimeglumine. *Magn. Reson. Imaging 27*, 101−107.

(38) Weinmann, H. J., Bauer, H., Frenzel, T., Muhler, A., and Ebert, W. (1996) Mechanism of hepatic uptake of gadoxetate disodium. *Acad Radiol. 3* (Suppl. 2), 232–234.

(39) Tsuda, N., Harada, K., and Matsui, O. (2011) Effect of change in transporter expression on gadolinium-ethoxybenzyl-diethylenetriamine pentaacetic acid-enhanced magnetic resonance imaging during hepatocarcinogenesis in rats. *J. Gastroenterol. Hepatol. 26*, 568–576.

(40) Van Beers, B. E., Pastor, C. M., and Hussain, H. K. (2012) Primovist, eovist: What to expect? *J. Hepatol. 57*, 421−429.

(41) Vilgrain, V., Van Beers, B. E., and Pastor, C. M. (2016) Insights into the diagnosis of hepatocellular carcinomas with hepatobiliary MRI. *J. Hepatol. 64*, 708−716.

(42) Kim, R. B. (2003) Organic anion-transporting polypeptide (OATP) transporter family and drug disposition. *Eur. J. Clin. Investig. 33* (Suppl. 2), 1–5.

(43) Veronika, B. A., Lena, S., Martin, S., Valentinos, K., Evangelos, B,, Andreas, G. T., Walter, J., and Theresia, T. (2013) Tumor-Specific Expression of Organic Anion-Transporting Polypeptides: Transporters as Novel Targets for Cancer Therapy. *Journal of Drug Delivery 2013*, 1–12.

(44) Battisti, M. U., Jozwiak, K., Cannazza, G., Puia, G., Stocca, G., Braghiroli, D., Parenti, C., Brasili, L., Carrozzo, M. M., Citti, C., et al. (2012) 5-Arylbenzothiadiazine Type Compounds as Positive Allosteric Modulators of AMPA/Kainate Receptors. *ACS Med. Chem. Lett*. 3, 25-29.

(45) Gui, C., and Hagenbuch, B. (2008) Amino Acid Residues in Transmembrane Domain 10 of Organic Anion Transporting Polypeptide 1B3 Are Critical for Cholecystokinin Octapeptide Transport. *Biochemistry 47,* 9090−9097.

(46) Ausch, B. V., Secky, L., Wlcek, K., Svoboda, M., Kounnis, V., Briasoulis, E., Tzakos, G. A., Jaeger, W., and Thalhammer, T. (2013) Tumor-specific expression of organic anion-transporting polypeptides: Transporters as novel target for cancer therapy. *Journal of drug delivery 2013*, 1-12.

(47) MacRenaris, K. W., Ma, Z., Krueger, R. L., Carney, C. E., and Meade, T. J. (2016) Cell-permeable esterase-activated Ca (II)-sensitive MRI contrast agent. *Bioconjugate Chem*. *27*, 465−473.

(48) Kim, H. K., Kang, M. K., Jung, K. H., Kang, S. H., Kim, Y. H., Jung, J. C., Lee, G. H., Chang, Y., and Kim, T. J. (2013) Gadolinium complex of DO3A-benzothiazole aniline (BTA) conjugate as a theranostic agent. *J. Med. Chem. 56*, 8104−8111.

(49) Jung, K. H., Kim, H-K., Park, J.-A., Nam, K. S., Lee, G. H., Chang, Y. and Kim, T-J., (2012) Gd Complexes of DO3A-(Biphenyl-2,2'-bisamides) Conjugates as MRI Blood-Pool Contrast Agents. *ACS Med. Chem. Lett*. *3*, 1003-1007.

(50) Xue, S., Yang, H., Qiao, J., Pu, F., Jiang, J., Hubbard, K., Hekmatyar, K., Langley, J., Salarian, M., Long, R. C. at al. (2015) Protein MRI contrast agent with unprecedented metal selectivity and sensitivity for liver cancer imaging. *Proc. Natl. Acad. Sci. U.S.A. 112* (21), 6607-6612.

(51) Zha, Z., Deng, Z., Li, Y., Li, C., Wang, J., Wang, S., Qu, E. and Dai, Z. (2013) Biocompatible polypyrrole nanoparticles as a novel organic photoacoustic contrast agent for deep tissue imaging. *Nanoscale 5*, 4462-4467.

(52) Lokling, K. E., Fossheim, S. L., Klaveness, J., and Skurtveit, R. (2004) Biodistribution of pH-responsive liposomes for MRI and a novel approach to improve the pH-responsiveness. *J. Controlled Release 98*, 87−95.

(53) Rohrer, M., Bauer, H., Mintorovitch, J., Requardt, M., and Weinmann, H. J. (2005) Comparison of Magnetic Properties of MRI Contrast Media Solutions at Different Magnetic Field Strengths. *Invest. Radiol. 40* (11), 715−724.

(54) Wiener, E., Woertler, K., Weirich, G., Rummeny, E. J. and Settles, M. (2007) Contrast enhanced cartilage imaging: Comparison of ionic and non-ionic contrast agents. *European Journal of Radiology 63*, 110−119.

(55) Schrödinger Release 2018-1: (2018) Prime, Schrödinger, LLC, New York, NY.

(56) Schrödinger Release 2018-1: (2018) Glide, Schrödinger, LLC, New York, NY.

Table of Contents Graphic